This paper is published as part of a *Nanoscale* themed issue on doped nanostructures

Guest Editor: Stephen Pearton

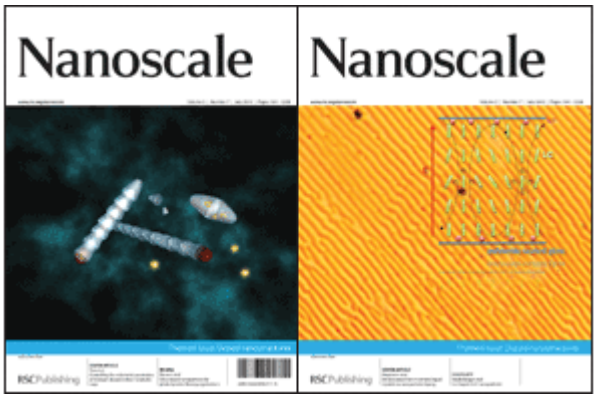

Editorial

Doped nanostructures
Stephen Pearton, *Nanoscale*, 2010
DOI: 10.1039/c005273f

Review Articles

Impacts of doping on thermal and thermoelectric properties of nanomaterials
Gang Zhang and Baowen Li, *Nanoscale*, 2010
DOI: 10.1039/c0nr00095g

Effect of N/B doping on the electronic and field emission properties for carbon nanotubes, carbon nanocones, and graphene nanoribbons
Shan-Sheng Yu and Wei-Tao Zheng, *Nanoscale*, 2010
DOI: 10.1039/c0nr00002g

Silica-based nanoparticles for photodynamic therapy applications
Pierre Couleaud, Vincent Morosini, Céline Frochot, Sébastien Richeter, Laurence Raehm and Jean-Olivier Durand, *Nanoscale*, 2010
DOI: 10.1039/c0nr00096e

Mini Review

Co-Doped ZnO nanoparticles: Minireview
Igor Djerdj, Zvonko Jagli?i?, Denis Ar?on and Markus Niederberger, *Nanoscale*, 2010
DOI: 10.1039/c0nr00148a

Communications

Controlling the volumetric parameters of nitrogen-doped carbon nanotube cups
Brett L. Allen, Matthew B. Keddie and Alexander Star, *Nanoscale*, 2010
DOI: 10.1039/c0nr00043d

Visible light induced photobleaching of methylene blue over melamine-doped TiO_2 nanocatalyst
Jurate Virkutyte, Babita Baruwati and Rajender S. Varma, *Nanoscale*, 2010
DOI: 10.1039/c0nr00089b

Selective detection of trace amount of Cu^{2+} using semiconductor nanoparticles in photoelectrochemical analysis
Guang-Li Wang, Jing-Juan Xu and Hong-Yuan Chen, *Nanoscale*, 2010
DOI: 10.1039/c0nr00084a

Flower-like TiO_2 nanosructures with exposed {001} facets: Facile synthesis and enhanced photocatalysis
Min Liu, Lingyu Piao, Weiming Lu, Siting Ju, Lei Zhao, Chunlan Zhou, Hailing Li and Wenjing Wang, *Nanoscale*, 2010
DOI: 10.1039/c0nr00050g

Papers

Electroconvection in nematic liquid crystals *via* nanoparticle doping
Martin Urbanski, Brandy Kinkead, Hao Qi, Torsten Hegmann and Heinz-S. Kitzerow, *Nanoscale*, 2010
DOI: 10.1039/c0nr00139b

Superhydrophilicity-assisted preparation of transparent and visible light activated N-doped titania film
Qing Chi Xu, Diana V. Wellia, Rose Amal, Dai Wei Liao, Say Chye Joachim Loo and Timothy Thatt Yang Tan, *Nanoscale*, 2010
DOI: 10.1039/c0nr00105h

The influence of doping on the device characteristics of $In_{0.5}Ga_{0.5}As/GaAs/Al_{0.2}Ga_{0.8}As$ quantum dots-in-a-well infrared photodetectors
G. Jolley, L. Fu, H. H. Tan and C. Jagadish, *Nanoscale*, 2010
DOI: 10.1039/c0nr00128g

Study of concentration-dependent cobalt ion doping of TiO_2 and $TiO_{2-x}N_x$ at the nanoscale
James L. Gole, Sharka M. Prokes, O. J. Glembocki, Junwei Wang, Xiaofeng Qiu and Clemens Burda, *Nanoscale*, 2010
DOI: 10.1039/c0nr00125b

Multifunctional nanocomposites of superparamagnetic (Fe_3O_4) and NIR-responsive rare earth-doped up-conversion fluorescent ($NaYF_4$: Yb,Er) nanoparticles and their applications in biolabeling and fluorescent imaging of cancer cells
Congcong Mi, Jingpu Zhang, Huanyu Gao, Xianlong Wu, Meng Wang, Yingfan Wu, Yueqin Di, Zhangrun Xu, Chuanbin Mao and Shukun Xu, *Nanoscale*, 2010
DOI: 10.1039/c0nr00102c

Effect of doping on the morphology and multiferroic properties of $BiFeO_3$ nanorods
Dimple P. Dutta, O. D. Jayakumar, A. K. Tyagi, K. G. Girija, C. G. S. Pillai and G. Sharma, *Nanoscale*, 2010
DOI: 10.1039/c0nr00100g

Effect of substrate temperature on implantation doping of Co in CdS nanocrystalline thin films
S. Chandramohan, A. Kanjilal, S. N. Sarangi, S. Majumder, R. Sathyamoorthy, C.-H. Hong and T. Som, *Nanoscale*, 2010
DOI: 10.1039/c0nr00123f

Modification of neodymium-doped ZnO hybrid nanoparticles under mild hydrothermal conditions
Behzad Shahmoradi, K. Soga, S. Ananda, R. Somashekar and K. Byrappa, *Nanoscale*, 2010
DOI: 10.1039/c0nr00069h

***Ex situ* vapor phase boron doping of silicon nanowires using BBr_3**
Gregory S. Doerk, Gabriella Lestari, Fang Liu, Carlo Carraro and Roya Maboudian, *Nanoscale*, 2010
DOI: 10.1039/c0nr00127a

Change in conformation of polymer PFO on addition of multiwall carbon nanotubes
Malti Bansal, Ritu Srivastava, C. Lal, M. N. Kamalasanan and L. S. Tanwar, *Nanoscale*, 2010
DOI: 10.1039/c0nr00001a

Amino acid-assisted one-pot assembly of Au, Pt nanoparticles onto one-dimensional ZnO microrods
Xianghong Liu, Jun Zhang, Xianzhi Guo, Shihua Wu and Shurong Wang, *Nanoscale*, 2010
DOI: 10.1039/c0nr00015a

Luminescence resonance energy transfer from an upconverting nanoparticle to a fluorescent phycobiliprotein
Fiorenzo Vetrone, Rafik Naccache, Christopher G. Morgan and John A. Capobianco, *Nanoscale*, 2010
DOI: 10.1039/c0nr00126k

Doping single-walled carbon nanotubes through molecular charge-transfer: a theoretical study
Arun K. Manna and Swapan K. Pati, *Nanoscale*, 2010
DOI: 10.1039/c0nr00124d

Energy transfer study between Ce^{3+} and Tb^{3+} ions in doped and core-shell sodium yttrium fluoride nanocrystals
Pushpal Ghosh, Arik Kar and Amitava Patra, *Nanoscale*, 2010
DOI: 10.1039/c0nr00019a

Pt surface modification of SnO_2 nanorod arrays for CO and H_2 sensors
Hui Huang, C. Y. Ong, J. Guo, T. White, M. S. Tse and O. K. Tan, *Nanoscale*, 2010
DOI: 10.1039/c0nr00159g

Poly (acrylic acid)-capped lanthanide-doped BaFCl nanocrystals: synthesis and optical properties
Qiang Ju, Wenqin Luo, Yongsheng Liu, Haomiao Zhu, Renfu Li and Xueyuan Chen, *Nanoscale*, 2010
DOI: 10.1039/c0nr00116c

Enhanced Cu emission in ZnS : Cu,Cl/ZnS core–shell nanocrystals
Carley Corrado, Morgan Hawker, Grant Livingston, Scott Medling, Frank Bridges and Jin Z. Zhang, *Nanoscale*, 2010
DOI: 10.1039/c0nr00056f

Synthesis and characterization of zirconium-doped mesoporous nano-crystalline TiO_2
Kanattukara Vijayan Bineesh, Dong-Kyu Kim and Dae-Won Park, *Nanoscale*, 2010
DOI: 10.1039/c0nr00108b

Zn-doped nanocrystalline TiO_2 films for CdS quantum dot sensitized solar cells
Guang Zhu, Zujun Cheng, Tian Lv, Likun Pan, Qingfei Zhao and Zhuo Sun, *Nanoscale*, 2010
DOI: 10.1039/c0nr00087f

Effect of synergy on the visible light activity of B, N and Fe co-doped TiO_2 for the degradation of MO
Mingyang Xing, Yongmei Wu, Jinlong Zhang and Feng Chen, *Nanoscale*, 2010
DOI: 10.1039/c0nr00078g

Facile synthesis of lanthanide nanoparticles with paramagnetic, down- and up-conversion properties
Zhengquan Li and Yong Zhang, *Nanoscale*, 2010
DOI: 10.1039/c0nr00073f

Glucose oxidase-doped magnetic silica nanostrutures as labels for localized signal amplification of electrochemical immunosensors
Jingjing Ren, Dianping Tang, Biling Su, Juan Tang and Guonan Chen, *Nanoscale*, 2010
DOI: 10.1039/b9nr00416e

The role of ellipticity on the preferential binding site of Ce and La in C_{78}-D_{3h}—A density functional theory study
K. Muthukumar and J. A. Larsson, *Nanoscale*, 2010
DOI: 10.1039/c0nr00021c

Tuning the shape and thermoelectric property of PbTe nanocrystals by bismuth doping
Qian Zhang, Ting Sun, Feng Cao, Ming Li, Minghui Hong, Jikang Yuan, Qingyu Yan, Huey Hoon Hng, Nianqiang Wu and Xiaogang Liu, *Nanoscale*, 2010
DOI: 10.1039/c0nr00115e

Effect of doping on the morphology and multiferroic properties of $BiFeO_3$ nanorods

Dimple P. Dutta,*[a] O. D. Jayakumar,[a] A. K. Tyagi,*[a] K. G. Girija,[a] C. G. S. Pillai[a] and G. Sharma[b]

Received 9th February 2010, Accepted 31st March 2010
First published as an Advance Article on the web 25th May 2010
DOI: 10.1039/c0nr00100g

In this study we report the synthesis of $BiFeO_3$ nanorods using a sonochemical technique. The nanorods had a diameter of 20–50 nm, a length of 100–500 nm and exhibit aspect ratios in the range of 5–10. However, after doping, the TEM images of $Bi_{0.9}Ba_{0.1}Fe_{0.9}Mn_{0.1}O_3$ and $Bi_{0.9}Ca_{0.1}Fe_{0.9}Cr_{0.1}O_3$ samples show that the aspect ratios of both the double doped samples have reduced considerably, while retaining the crystallinity of the particles. $BiFeO_3$ nanorods show a weak ferromagnetic order at room temperature, which is quite different from the linear M–H relationship reported for bulk $BiFeO_3$. The saturation magnetization of these $BiFeO_3$ nanostructures has been found to increase on doping with various metal ions (Ba^{2+}, Ca^{2+}, Mn^{2+}, Cr^{3+}), reaching a maximum value of 1.35 emu g^{-1} for the $Bi_{0.9}Ba_{0.1}Fe_{0.9}Mn_{0.1}O_3$ nanostructures. However, saturation of electric polarization was observed only in case of the $Bi_{0.9}Ca_{0.1}Fe_{0.9}Cr_{0.1}O_3$ nanostructures.

Introduction

Multiferroic materials yield simultaneous effects of ferroelectricity, ferromagnetism or ferroelasticity in the same material due to their unique and strong coupling of electric, magnetic, and structural order parameters.[1,2] Hence, they offer a wide opportunity for potential applications in information storage, magnetic recording media, spintronic devices and sensors.[3–5] Among all the multiferroic materials studied so far, $BiFeO_3$ (BFO) which exhibits the coexistence of ferroelectric and antiferromagnetic (AFM) orders has received great attention as it has the potential to be one of the prime candidates for room-temperature magneto electric applications due to its high ferroelectric Curie point ($T_C \sim 1103$ K) and the antiferromagnetic (AFM) Néel point ($T_N \sim 647$ K). However, both its spontaneous polarization and saturation magnetization are disappointingly low when compared to many standard ferroelectrics and ferromagnets. This is due to the superimposition of a spiral spin structure on BFO's antiferromagnetic order. In this spiral spin structure, the antiferromagnetic axis rotates through the crystal with an incommensurate long-wavelength period of 62 nm, which cancels the macroscopic magnetization and also inhibits the observation of the linear magnetoelectric effect in bulk BFO.[6,7] Hence, for novel electronics applications of BFO, its magnetic and electric properties must be enhanced.

Several studies aimed at upgrading the magnetic and ferroelectric properties of $BiFeO_3$ have ensued in the last five years. Improvement in magnetic properties at room temperature has been observed in single crystalline bismuth ferrite nanoparticles which show strong size-dependent magnetic properties.[8–10] Also the ferroelectric saturation polarization P_s and remnant polarization P_r of $BiFeO_3$ nanoparticles have been reported to be higher than that of the bulk material.[11] Introducing suitable dopant ions in $BiFeO_3$ films has also been reported to be a potential method for enhancing its magnetic, electric and magnetoelectric properties.[5,12–17] Hence it was of interest to synthesize doped $BiFeO_3$ nanoparticles and study the effect of the dopant ions on its magnetic and electric properties at room temperature.

It has always been a challenge to synthesize pure $BiFeO_3$ as the product is mostly contaminated with secondary phases such as Bi_2O_3 and $Bi_2Fe_4O_9$.[18] In the present work, we have synthesized phase pure undoped $BiFeO_3$ and co-doped $Bi_{0.9}Ba_{0.1}Fe_{0.9}Mn_{0.1}O_3$ and $Bi_{0.9}Ca_{0.1}Fe_{0.9}Cr_{0.1}O_3$ nanostructures through a sonochemical route. Sonochemical synthesis is based on acoustic cavitation resulting from the continuous formation, growth and implosive collapse of the bubbles in a liquid.[19,20] Undoped $BiFeO_3$ nanoparticles synthesized using the sonochemical technique has been reported earlier but the products showed the presence of some unidentified peaks in the powder X-ray diffraction pattern.[21] The choice of the dopant ions was based on the fact that replacing Fe^{3+} ions in $BiFeO_3$ thin films with other transition metal ions such as Cr^{3+} and Mn^{3+} that have better electronic stability is expected to increase the resistance by reducing valence fluctuations in Fe^{3+}.[22–25] Also, weak ferromagnetism has been observed at room temperature for single doped $BiFeO_3$ nanoparticles where divalent cations, *viz*. Ba^{2+} and Ca^{2+}, substitute trivalent cations of Bi^{3+}.[26] We have also evaluated the magnetic and ferroelectric properties of the sonochemically synthesized $Bi_{0.9}Ba_{0.1}Fe_{0.9}Mn_{0.1}O_3$ and $Bi_{0.9}Ca_{0.1}Fe_{0.9}Cr_{0.1}O_3$ nanoparticles and the details of this work are discussed herein.

Results and discussion

Undoped $BiFeO_3$, single doped $BiFeO_3$ ($Bi_{0.9}Ba_{0.1}FeO_3$, $BiFe_{0.9}Mn_{0.1}O_3$, $Bi_{0.9}Ca_{0.1}FeO_3$, $BiFe_{0.9}Cr_{0.1}O_3$) and double doped $BiFeO_3$ ($Bi_{0.9}Ba_{0.1}Fe_{0.9}Mn_{0.1}O_3$, $Bi_{0.9}Ca_{0.1}Fe_{0.9}Cr_{0.1}O_3$) particles were synthesized using the sonochemical technique. The XRD patterns of the undoped $BiFeO_3$ as well as that of

[a]*Chemistry Division, Bhabha Atomic Research Centre, Mumbai, 400085, India. E-mail: dimpled@barc.gov.in; aktyagi@barc.gov.in*
[b]*Mechanical Metallurgy Section, Bhabha Atomic Research Centre, Mumbai, 400085, India*

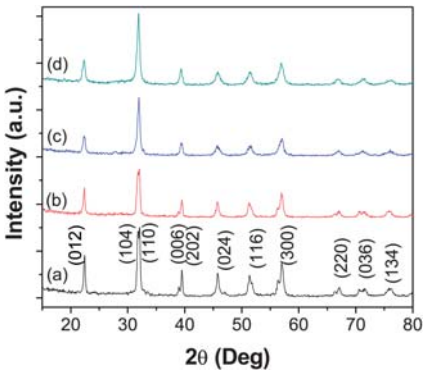

Fig. 1 XRD patterns of (a) $BiFeO_3$, (b) $Bi_{0.9}Ba_{0.1}FeO_3$, (c) $BiFe_{0.9}Mn_{0.1}O_3$ and (d) $Bi_{0.9}Ba_{0.1}Fe_{0.9}Mn_{0.1}O_3$.

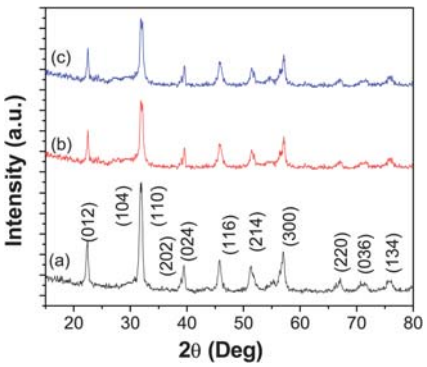

Fig. 2 XRD patterns of (a) $Bi_{0.9}Ca_{0.1}FeO_3$, (b) $BiFe_{0.9}Cr_{0.1}O_3$, and (c) $Bi_{0.9}Ca_{0.1}Fe_{0.9}Cr_{0.1}O_3$.

$Bi_{0.9}Ba_{0.1}FeO_3$, $BiFe_{0.9}Mn_{0.1}O_3$ and $Bi_{0.9}Ba_{0.1}Fe_{0.9}Mn_{0.1}O_3$ are shown in Fig. 1, while those of $Bi_{0.9}Ca_{0.1}FeO_3$, $BiFe_{0.9}Cr_{0.1}O_3$ and $Bi_{0.9}Ca_{0.1}Fe_{0.9}Cr_{0.1}O_3$ are shown in Fig. 2, respectively. The peaks in all the XRD pattern corresponded to the rhombohedral structure of $BiFeO_3$ with R_{3c} space group (JCPDS no: 71-2494). The observed broadening of the peaks in the XRD patterns of all the above samples, compared to that normally seen for bulk $BiFeO_3$ obtained *via* solid state synthesis is typical for nanoparticles. No additional peaks were observed in any of the XRD patterns, confirming the formation of phase pure $BiFeO_3$. Earlier reports on alkaline earth metal doped $BiFeO_3$ nanoparticles synthesized using a sol–gel technique showed the presence of some unidentified impurity phases.[26] The lattice parameters of all the samples are given in Table 1. The lattice parameters of undoped $BiFeO_3$ is relatively close to the reported literature values (a = 5.587 Å, c = 13.860 Å). However, the lattice parameter values change on doping $BiFeO_3$. The results suggest that the rhombohedral $BiFeO_3$ structure undergoes distortion on doping, which involves Fe or Bi displacements relative to the cubic perovskite parent structure. The (104) and (110) peaks are overlapping in case of $BiFe_{0.9}Mn_{0.1}O_3$ and $Bi_{0.9}Ba_{0.1}Fe_{0.9}Mn_{0.1}O_3$, but can be distinguished in pure $BiFeO_3$ and for all the other doped samples.

Table 1 Structural parameters of undoped and doped $BiFeO_3$ samples

Sample	a/Å	c/Å
$BiFeO_3$	5.5811(1)	13.8589(2)
$Bi_{0.9}Ba_{0.1}FeO_3$	5.5799(2)	13.8575(1)
$BiFe_{0.9}Mn_{0.1}O_3$	5.5817(4)	13.8598(1)
$Bi_{0.9}Ba_{0.1}Fe_{0.9}Mn_{0.1}O_3$	5.5778(5)	13.8264(2)
$Bi_{0.9}Ca_{0.1}FeO_3$	5.5673(5)	13.7712(3)
$BiFe_{0.9}Cr_{0.1}O_3$	5.5713(3)	13.7932(5)
$Bi_{0.9}Ca_{0.1}Fe_{0.9}Cr_{0.1}O_3$	5.5768(5)	13.8231(4)

To further investigate the microstructure and topography, we used transmission electron microscope to image the undoped and doped $BiFeO_3$ samples on carbon coated copper TEM grids. Fig. 3A shows the TEM image of undoped $BiFeO_3$ sample obtained *via* sonochemical synthesis followed by heat treatment at 400 °C for 1 h. It can be seen that the obtained nanocrystalline $BiFeO_3$ are rod-like with a diameter of 20–50 nm and a length of 100–500 nm. These pure $BiFeO_3$ nanorods exhibit aspect ratio in the range of 5–10. There are reports on faceted $BiFeO_3$ nanoparticles synthesized using a sol–gel technique, nanospindles synthesized using a hydrothermal route and also nanowires and nanotubes synthesized using template assisted synthesis.[8,27–29] However, to the best of our knowledge, this is the first report on the synthesis of $BiFeO_3$ nanorods. The energy dispersive spectrum of the $BiFeO_3$ nanorods shown in Fig. 4 confirms the presence of Bi, Fe and O in our prepared sample. The atomic ratio of Bi to Fe is approximately 1 : 1. Spectra taken at a number of selected positions of the sample show the presence of the same constituents. The Cu and C signals arise from the TEM grid. Fig. 3B shows the selected area electron diffraction (SAED) pattern taken from the $BiFeO_3$ nanorod, which exhibits its highly crystalline structure. The indexing of the concentric rings corresponds to the rhombohedral $BiFeO_3$ structure. The TEM images of $Bi_{0.9}Ba_{0.1}Fe_{0.9}Mn_{0.1}O_3$ and $Bi_{0.9}Ca_{0.1}Fe_{0.9}Cr_{0.1}O_3$ samples are

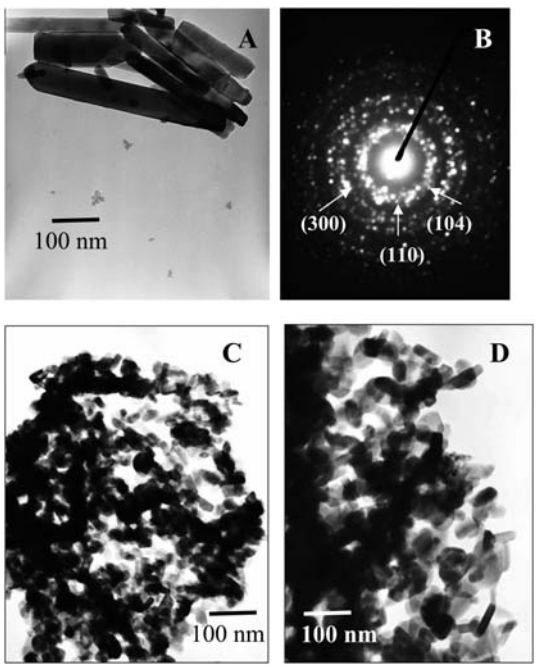

Fig. 3 (A) TEM image of $BiFeO_3$, (B) SAED pattern of $BiFeO_3$, (C) TEM image of $Bi_{0.9}Ba_{0.1}Fe_{0.9}Mn_{0.1}O_3$ and (D) TEM image of $Bi_{0.9}Ca_{0.1}Fe_{0.9}Cr_{0.1}O_3$.

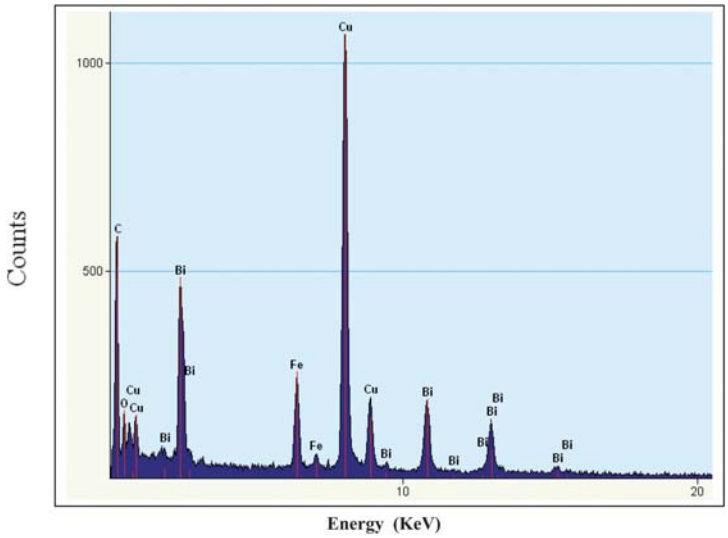

Fig. 4 EDX spectrum of $BiFeO_3$ nanorods showing Bi, Fe and O peaks. Note: The Cu and C peaks are due to the carbon coated copper grids used for dispersing the sample.

shown in Fig. 3C and 3D, respectively. It is clear from the images that the aspect ratios of both the double doped samples have reduced considerably, while retaining the crystallinity of the particles. In case of $Bi_{0.9}Ba_{0.1}Fe_{0.9}Mn_{0.1}O_3$, very few particles with a nanorod shape are seen, as a majority of them have a faceted morphology (Fig. 3C). Compared to $Bi_{0.9}Ba_{0.1}Fe_{0.9}Mn_{0.1}O_3$, the $Bi_{0.9}Ca_{0.1}Fe_{0.9}Cr_{0.1}O_3$ samples show the presence of more nanorods (Fig. 3D). This clearly indicates that the nanorod shape of the $BiFeO_3$ particles is destabilized under the influence of various dopant ions. Such an effect has also been observed in cobalt doped ZnO nanostructures.[30]

To investigate the magnetic order at room temperature of our undoped bismuth ferrite nanorods, magnetic measurements were done using vibrating sample magnetometer (VSM). For all the samples we can observe sizable hysteresis with a finite value of the coercive field, remanent magnetization and saturation magnetization that are tabulated in Table 2. A DC magnetization loop of the $BiFeO_3$ nanorods, recorded at 300 K, is shown in Fig. 5. The data represent the average of all random orientations of the $BiFeO_3$ nanorods used for the measurements. $BiFeO_3$ nanorods show a weak ferromagnetic order at room temperature, which is quite different from the linear M–H relationship reported for bulk $BiFeO_3$.[31] The weak ferromagnetic order was also observed in

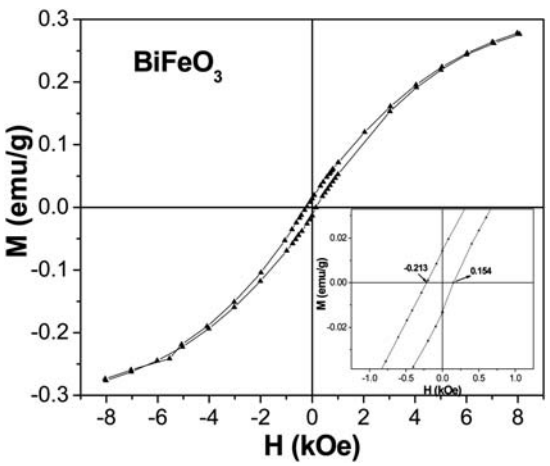

Fig. 5 Field variation of magnetization over ±8 kOe at room temperature for the undoped $BiFeO_3$ nanorods. Inset (right) enlarges $M(H)$ curve showing the presence of hysteresis.

Table 2 Magnetic parameters at room temperature

Sample	Coercive field/Oe	Remanant magnetization/ emu g^{-1}	Maximum magnetization (at 8 kOe)/ emu g^{-1}
$BiFeO_3$	382	0.01	0.28
$Bi_{0.9}Ba_{0.1}FeO_3$	1918	0.04	0.31
$BiFe_{0.9}Mn_{0.1}O_3$	574	0.02	0.32
$Bi_{0.9}Ba_{0.1}Fe_{0.9}Mn_{0.1}O_3$	1942	0.25	1.35
$Bi_{0.9}Ca_{0.1}FeO_3$	350	0.11	0.68
$BiFe_{0.9}Cr_{0.1}O_3$	350	0.05	0.47
$Bi_{0.9}Ca_{0.1}Fe_{0.9}Cr_{0.1}O_3$	1142	0.13	1.06

$BiFeO_3$ films, nanoparticles, nanowires and nanotubes.[26,28,29,32–34] The weak ferromagnetic order generally observed in BFO films and in nanoparticles has been attributed to the size effect. It is well known that the incommensurate spiral spin structure of bulk BFO, with a period of 62 nm, cancels the macroscopic magnetization. The BFO nanostructures with typical dimensions below 62 nm can possess favorable magnetic properties due to their grain size confinement, an effect that has been found to partially destroy the long-range spiral spin structure of bulk BFO. The diameters of our $BiFeO_3$ nanorods are in the range of 20–50 nm, which is less than the wavelength of the incommensurate spiral spin structure of the bulk material. This would lead to partial destruction of the spiral spin structure in the $BiFeO_3$ nanorods and hence the incomplete spin compensation becomes measurable, resulting in weak FM behaviors. The maximum magnetization, M_S, measured at the maximum applied field of $H_{appl} = 8$ kOe corresponds to $M_S \sim 0.277$ emu g^{-1} (0.016 μ_B/Fe) for the $BiFeO_3$

nanorods. This is less than that observed in case of $BiFeO_3$ nanowires ($M_S \sim 0.534$ emu g^{-1}) but more than that reported for $BiFeO_3$ nanotubes ($M_S \sim 0.125$ emu g^{-1}).[28,29] This may be attributed to the different shape anisotropy, magnetocrystalline anisotropy and different extents of defects present in the various nanoforms. The coercive field of the nanorods is quite small ($H_c \sim 382$ Oe). A shift in the hysteresis loops is also observed in the M–H curves of $BiFeO_3$ nanorods (shown as inset in Fig. 4). This can be ascribed to the presence of exchange coupling between the ferromagnetic surfaces and the antiferromagnetic cores. The hysteresis loops of undoped $BiFeO_3$ nanorods exhibit very small remnant magnetization and a lack of proper saturation. This can be attributed to the presence of exchange and dipolar interparticle interactions in our system.

Fig. 6 shows the room temperature magnetic hysteresis curves for the single doped $Bi_{0.9}Ba_{0.1}FeO_3$, $BiFe_{0.9}Mn_{0.1}O_3$ and double doped $Bi_{0.9}Ba_{0.1}Fe_{0.9}Mn_{0.1}O_3$ samples. There is a small increase in the maximum magnetization (M_S) of single doped $BiFeO_3$ nanostructures with Mn and Ba doping ($M_S \sim 0.31$ emu g^{-1}) compared to that observed in $BiFeO_3$ nanorods. These effects may originate from the variable valence and dissimilar transition metal ions. The highest value of M_S (1.35 emu g^{-1}), M_R (0.25 emu g^{-1}) and coercive field H_c (1.94 kOe) occurs in the double doped $Bi_{0.9}Ba_{0.1}Fe_{0.9}Mn_{0.1}O_3$ nanostructures. The high coercive field value obtained in case of single doped $Bi_{0.9}Ba_{0.1}FeO_3$ nanostructures was comparable to that reported for $Bi_{0.95}Ba_{0.05}FeO_3$ nanoparticles.[26] However, $Bi_{0.9}Ba_{0.1}FeO_3$ and $Bi_{0.9}Ba_{0.1}Fe_{0.8}Mn_{0.2}O_3$ samples synthesized *via* pyrolysis of xerogel precursors exhibited higher M_S and coercive field values compared to our nanostructures. This may be due to the presence of *P4mm* phase in their samples, which is absent in our case, since in systems like $BiFeO_3$, different synthesis methods often lead to different competing structures. The M–H loops for $Bi_{0.9}Ca_{0.1}FeO_3$, $BiFe_{0.9}Cr_{0.1}O_3$ and $Bi_{0.9}Ca_{0.1}Fe_{0.9}Cr_{0.1}O_3$ are shown in Fig. 7. In this case also, though the highest value of M_S (1.06 emu g^{-1}), M_R (0.13 emu g^{-1}) and coercive field H_c (1.14 kOe) occurs in the double doped $Bi_{0.9}Ba_{0.1}Fe_{0.9}Mn_{0.1}O_3$, it is less than that observed for $Bi_{0.9}Ba_{0.1}Fe_{0.9}Mn_{0.1}O_3$ nanostructures. $Bi_{0.9}Ca_{0.1}FeO_3$ show the highest M_S (0.68 emu g^{-1}) value among all the single doped samples though it is less than that reported for $Bi_{0.9}Ca_{0.1}FeO_3$ nanoparticles synthesized using a sol–gel route.[26]

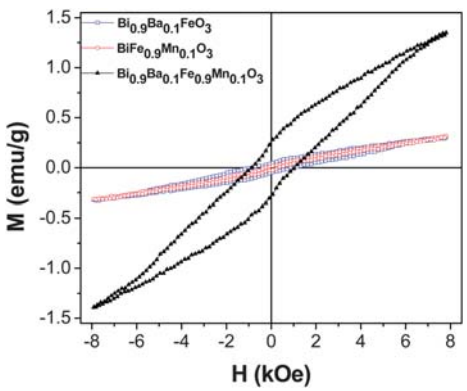

Fig. 6 Field variation of magnetization over ±8 kOe at room temperature for the $Bi_{0.9}Ba_{0.1}FeO_3$, $BiFe_{0.9}Mn_{0.1}O_3$ and $Bi_{0.9}Ba_{0.1}Fe_{0.9}Mn_{0.1}O_3$ samples.

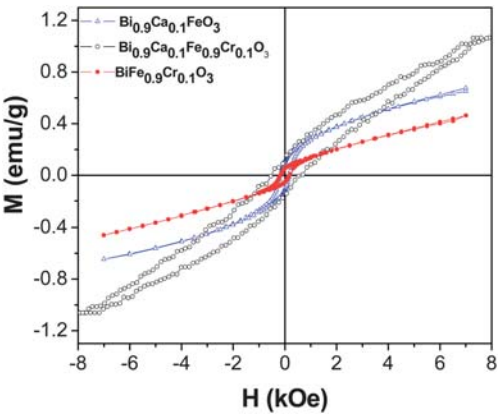

Fig. 7 Field variation of magnetization over ±8 kOe at room temperature for the $Bi_{0.9}Ca_{0.1}FeO_3$, $BiFe_{0.9}Cr_{0.1}O_3$ and $Bi_{0.9}Ca_{0.1}Fe_{0.9}Cr_{0.1}O_3$ samples.

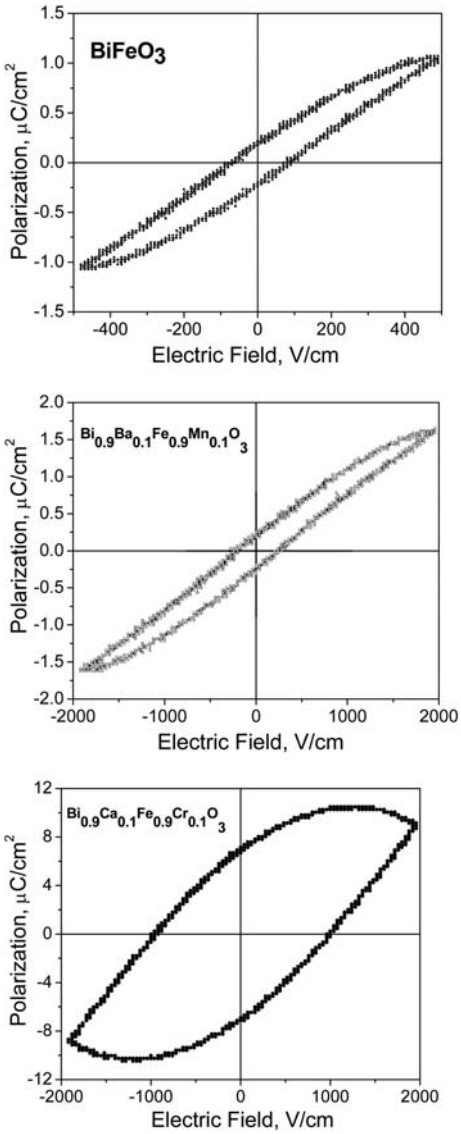

Fig. 8 FE hysteresis loop for $BiFeO_3$ nanorods, $Bi_{0.9}Ba_{0.1}Fe_{0.9}Mn_{0.1}O_3$ and $Bi_{0.9}Ca_{0.1}Fe_{0.9}Cr_{0.1}O_3$ nanostructures.

Fig. 8 shows the ferroelectric properties of the undoped $BiFeO_3$ nanorods and double doped $Bi_{0.9}Ba_{0.1}Fe_{0.9}Mn_{0.1}O_3$ and $Bi_{0.9}Ca_{0.1}Fe_{0.9}Cr_{0.1}O_3$ nanostructures, investigated by the *P–E* loop measurements. At a maximum applied electric field of ± 500 V cm^{-1}, the remanent polarization (P_r) is 0.21 μC cm^{-2} and the coercive field (E_c) is 155 V cm^{-1} for the $BiFeO_3$ nanorods. The P_r value is much less than that reported in case of $BiFeO_3$ nanoparticles and thin films, but higher than that observed in case of bulk $BiFeO_3$.[11,35,36] Saturation of polarization is not observed in case of the $BiFeO_3$ nanorods as well as $Bi_{0.9}Ba_{0.1}Fe_{0.9}Mn_{0.1}O_3$ nanostructures at a maximum applied electric field of ± 500 V cm^{-1} and ± 2000 V cm^{-1}, respectively. However, a high saturation polarization (P_s) of 10.5 μC cm^{-2}, P_r of 7 μC cm^{-2} and E_c of 1957 V cm^{-1} is observed in case of the $Bi_{0.9}Ca_{0.1}Fe_{0.9}Cr_{0.1}O_3$ nanostructures. The *P–E* hysteresis loops of all samples indicate their ferroelectric nature but with lossy features. This leaky feature is the least in case of $Bi_{0.9}Ca_{0.1}Fe_{0.9}Cr_{0.1}O_3$.

To understand this behavior, we have to first note that in $BiFeO_3$, small amounts of Fe^{2+} ions and oxygen vacancies exist.[37] Incidentally, $BiFeO_3$ shows p-type conductivity,[38] which can be understood by considering the substitution of a small amount Fe^{2+} ions in Fe^{3+} positions (acceptor doping of Fe^{3+} by Fe^{2+}). When Ca^{2+}/Ba^{2+} and Cr^{3+}/Mn^{2+} is added to $BiFeO_3$, Ca^{2+}/Ba^{2+} is supposed to substitute Bi^{3+} because of the close ionic radii of Ca^{2+}/Ba^{2+} and Bi^{3+}. Such acceptor doping of Bi^{3+} by Ca^{2+}/Ba^{2+} is expected to generate oxygen vacancies without the liberation of electrons.[39] Normally, the oxygen partial pressure in the ambience is sufficient to incorporate oxygen into the structure to nullify the oxygen vacancies and show p-type conductivity. The hole generated can be consumed by Fe^{2+} in Fe^{3+} position resulting in lower acceptor doping of Fe^{3+} by Fe^{2+} in $BiFeO_3$ with consequent decrease in conductivity. When Cr^{3+} substitutes Fe^{3+}, the acceptor doping of Fe^{3+} by Fe^{2+} is further reduced since Cr^{3+} is very stable electronically and this further causes a decrease in the conductivity. Hence, Ca^{2+} and Cr^{3+} co-doped $BiFeO_3$ show comparatively non-lossy ferroelectric hysteresis loops compared to undoped $BiFeO_3$ and $Bi_{0.9}Ba_{0.1}Fe_{0.9}Mn_{0.1}O_3$ nanostructures.

Experimental

All the reactions were carried out at room temperature under ambient conditions. High purity bismuth nitrate [$Bi(NO_3)_3\cdot 5H_2O$], ferric nitrate [$Fe(NO_3)_3\cdot 9H_2O$], manganese acetate [$Mn(OOCCH_3)_2\cdot 4H_2O$], chromium nitrate [$Cr(NO_3)_3\cdot 9H_2O$], barium nitrate [$Ba(NO_3)_2$] and calcium chloride [$CaCl_2$] were obtained from commercial sources (Aldrich). In a typical procedure, an aqueous solution of $Bi(NO_3)_3\cdot 6H_2O$ and $Fe(NO_3)_3\cdot 9H_2O$ was sonicated for 20 min. To the mixture, 5 ml of tetraethylene glycol (TEG) was added and sonicated for further 10 min. The pH of the solution was then adjusted to ~8 by adding ammonia solution and the resultant mixture was irradiated with a high intensity (100 W cm^{-2}) ultrasonic radiation operating at 20 kHz, under air at room temperature for 100 min. This was done by the direct immersion of a titanium horn (13 mm diameter) to a depth of 6 cm in the solution. The subsequently formed white precipitate was centrifuged, washed with distilled water and finally with acetone. The product was heated under air in furnace at 400 °C for 1 h.

For the doped $BiFeO_3$ nanostructures, the method is similar to that reported for undoped $BiFeO_3$ but here a stoichiometric amount of barium nitrate/manganese acetate or calcium chloride/chromium nitrate was also added to the reaction mixture. We have prepared $Bi_{0.9}Ba_{0.1}FeO_3$, $BiFe_{0.9}Mn_{0.1}O_3$, $Bi_{0.9}Ba_{0.1}Fe_{0.9}Mn_{0.1}O_3$, $Bi_{0.9}Ca_{0.1}FeO_3$, $BiFe_{0.9}Cr_{0.1}O_3$ and $Bi_{0.9}Ca_{0.1}Fe_{0.9}Cr_{0.1}O_3$ nanostructures using the sonochemical technique. The products obtained were subjected to thermal treatment, and resultant residues were characterized by XRD.

Characterization

X-Ray diffraction (XRD) measurements were carried out on a Philips Instrument, operating with Cu-Kα radiation (λ = 1.5406 Å) and employing a scan rate of 0.02° s^{-1} in the scattering angular range (2θ) of 15° to 80°. Silicon was used as an external standard for correction due to instrumental broadening. The average crystallite size was calculated from the diffraction line width based on Scherrer's relation: $d = 0.9\lambda/B\cos\theta$, where λ denotes the wavelength of X-rays and B is the corrected full width at half maxima (FWHM). EDS analyses was were carried out using an Inca Energy 250 instrument coupled to Vega MV2300t/40 scanning electron microscope. Conventional TEM micrographs were recorded on JEOL 2000FX. The particulates obtained, were dispersed in methanol solution and then deposited on the carbon coated copper grids for TEM/SAED studies. Magnetization of powder samples was measured using an EG&G P.A.R. vibrating sample magnetometer (model 4500). The magnetic hysteresis loops (*M vs. H*) was measured at 300 K with $H = \pm 8$ kOe. Electric field (*P–E*) hysteresis loops of the samples (5 mm diameter pellet with sputtered gold as top electrode and silver paste as bottom electrode) were measured by the modified Sawyer–Tower circuit at a 1 kHz ac frequency.

Conclusion

Phase pure $BiFeO_3$ nanorods have been successfully synthesized using a facile sonochemical technique. These nanorods show a weak ferromagnetic order at room temperature, which is quite different from the linear *M–H* relationship reported for bulk $BiFeO_3$. On doping, the nanorod shape of the $BiFeO_3$ particles is destabilized and we get nanostructures with a reduced aspect ratio. Addition of various dopants in $BiFeO_3$ nanorods, alters their magnetic as well as ferroelectric properties to different extents. The highest value of M_S (1.35 emu g^{-1}), M_R (0.25 emu g^{-1}) and coercive field H_c (1.94 kOe) occurs in the double doped $Bi_{0.9}Ba_{0.1}Fe_{0.9}Mn_{0.1}O_3$ nanostructures. However, saturation of electric polarization was observed only in case of $Bi_{0.9}Ca_{0.1}Fe_{0.9}Cr_{0.1}O_3$ which exhibited a P_s of 10.5 μC cm^{-2}, P_r of 7 μC cm^{-2} and E_c of 1957 V cm^{-1}. This material also showed enhanced ferromagnetic properties compared to the bulk $BiFeO_3$. Thus, fine tuning of the concentration of these dopants in $BiFeO_3$ nanostructures can lead to better materials for different potential applications.

References

1 H. Schmid, *Ferroelectrics*, 1994, **162**, 19–25.
2 W. Eerenstein, N. D. Mathur and J. F. Scott, *Nature*, 2006, **442**, 759–765.

3 M. Fiebig, T. Lottermoser, D. Fröhlich, A. V. Goltsev and R. V. Pisarev, *Nature*, 2002, **419**, 818–820.
4 N. Hur, S. Park, P. A. Sharma, J. S. Ahn, S. Guha and S.-W. Cheong, *Nature*, 2004, **429**, 392–395.
5 J. Wang, J. B. Neaton, H. Zheng, V. Nagarajan, S. B. Ogale, B. Liu, D. Viehland, V. Vaithyanathan, D. G. Schlom, U. V. Waghmare, N. A. Spaldin, K. M. Rabe, M. Wuttig and R. Ramesh, *Science*, 2003, **299**, 1719–1722.
6 I. Sosnowska, T. Peterlin-Neumaier and E. Streichele, *J. Phys. C: Solid State Phys.*, 1982, **15**, 4835.
7 Y. F. Popov, A. K. Zvezdin, G. P. Vorob'ev, A. M. Kadomtseva, V. A. Murashev and D. N. Rakov, *JETP Lett.*, 1993, **57**, 69.
8 Tae-J. Park, G. C. Papaefthymiou, A. J. Viescas, A. R. Moodenbaugh and S. S. Wong, *Nano Lett.*, 2007, **7**, 766–772.
9 R. Mazumder, S. Ghosh, P. Mondal, D. Bhattacharya, S. Dasgupta, N. Das, A. Sen, A. K. Tyagi, M. Sivakumar, T. Takami and H. Ikuta, *J. Appl. Phys.*, 2006, **100**, 033908.
10 R. Mazumder, P. S. Devi, D. Bhattacharya, P. Choudhury, A. Sen and M. Raja, *Appl. Phys. Lett.*, 2007, **91**, 062510.
11 Y.-Q. Kang, M.-S. Cao, J. Yuan and X.-L. Shi, *Mater. Lett.*, 2009, **63**, 1344–1346.
12 M. Azuma, K. Tanaka, T. Saito, S. Ishitwata, Y. Shimakawa and M. Takano, *J. Am. Chem. Soc.*, 2005, **127**, 8889.
13 J. B. Li, G. H. Ra, J. K. Liang, J. Luo and J. Chen, *Appl. Phys. Lett.*, 2007, **90**, 162513.
14 B. Yu, M. Li, J. Liu, D. Guo, L. Pei and X. Zhao, *J. Phys. D: Appl. Phys.*, 2008, **41**, 065003.
15 G. l. Yuan, S. O. Wing and H. L. W. Chan, *J. Appl. Phys.*, 2007, **101**, 064101.
16 D. H. Wang, W. C. Goh, M. Ning and C. K. Ong, *Appl. Phys. Lett.*, 2006, **88**, 212907.
17 V. A. Khomchenko, D. A. Kiselev, J. M. Vieira, A. L. Kholkin, M. A. Sá and Y. G. Pogorelov, *Appl. Phys. Lett.*, 2007, **90**, 242901.
18 J.-C. Chen and J.-M. Wu, *Appl. Phys. Lett.*, 2007, **91**, 182903.
19 S. Sundar Manoharan and M. Rao, *Encyclopedia of Nanoscience and Nanotechnology*, ed. H. S. Nalwa, American Scientific Publishers, USA, p. 67.
20 K. S. Suslick, *Science*, 1990, **247**, 1439.
21 N. Das, R. Majumdar, A. Sen and H. S. Maiti, *Mater. Lett.*, 2007, **61**, 2100–2104.
22 J. K. Kim, S. S. Kim, W.-J. Kim, A. S. Balla and R. Guo, *Appl. Phys. Lett.*, 2006, **88**, 132901.
23 S. U. Lee, S. S. Kim, H. K. Jo, M. H. Park, J. W. Kim and A. S. Bhalla, *J. Appl. Phys.*, 2007, **102**, 044107.
24 D. H. Kim, H. N. Lee, M. D. Biegalski and H. M. Christen, *Appl. Phys. Lett.*, 2007, **91**, 042906.
25 M. Azuma, H. Kanda, A. A. Belik, Y. Shimakawa and M. Takano, *J. Magn. Magn. Mater.*, 2007, **310**, 1177.
26 B. Bhushan, A. Basumallick, S. K. Bandopadhyay, N. Y. Vasanthacharya and D. Das, *J. Phys. D: Appl. Phys.*, 2009, **42**, 065004.
27 J.-T. Han, Y.-H. Huang, X.-J. Wu, C.-L. Wu, W. Wei, B. Peng, W. Huang and J. B. Goodenough, *Adv. Mater.*, 2006, **18**, 2145–2148.
28 J. Wei, D. Xue and Y. Xu, *Scr. Mater.*, 2008, **58**, 45–48.
29 F. Gao, Y. Yuan, K. F. Wang, X. Y. Chen, F. Chen and J. M. Liu, *Appl. Phys. Lett.*, 2006, **89**, 102506.
30 O. D. Jayakumar, C. Sudakar, C. Persson, V. Sudarsan, T. Sakuntala, R. Naik and A. K. Tyagi, *Cryst. Growth Des.*, 2009, **9**, 4450–4455.
31 S. T. Zhang, M. H. Lu, D. Wu, Y. F. Chen and N. B. Ming, *Appl. Phys. Lett.*, 2005, **87**, 262907.
32 F. Gao, X. Chen, K. Yin, S. Dong, Z. Ren, F. Yuan, T. Yu, Z. Zou and J.-M. Liu, *Adv. Mater.*, 2007, **19**, 2889–2892.
33 P. Kharel, S. Talebi, B. Ramachandran, A. Dixit, V. M. Naik, M. B. Sahana, C. Sudakar, R. Naik, M. S. R. Rao and G. Lawes, *J. Phys.: Condens. Matter*, 2009, **21**, 036001.
34 O. D. Jayakumar, S. N. Achary, K. G. Girija, A. K. Tyagi, C. Sudakar, G. Lawes, R. Naik, J. Nisar, X. Peng and R. Ahuja, *Appl. Phys. Lett.*, 2010, **96**, 032903.
35 V. R. Palkar, J. John and R. Pinto, *Appl. Phys. Lett.*, 2002, **80**, 1628–1630.
36 M. M. Kumar, V. R. Palkar, K. Srinivas and S. V. Suryanarayana, *Appl. Phys. Lett.*, 2000, **76**, 2764–2766.
37 V. R. Palkar and R. Pinto, *Pramana*, 2002, **58**, 1003.
38 A. S. Poghossian, H. V. Abovian, P. B. Avakian, S. H. Mkrtchian and V. M. Haroutunian, *Sens. Actuators, B*, 1991, **4**, 545.
39 A. J. Moulson and J. M. Herbert, *Electroceramics: Materials, Properties & Application*, Chapman & Hall, London, 1997.

